Volume 4 | Number 11 | November 2020

MATERIALS CHEMISTRY

FRONTIERS

CCS 中国化学会 CHINESE CHEMICAL SOCIETY

ICCAS 1956 中国科学院化学研究所 CHINESE ACADEMY OF SCIENCES

ROYAL SOCIETY OF CHEMISTRY

rsc.li/frontiers-materials

MATERIALS CHEMISTRY FRONTIERS

RESEARCH ARTICLE

View Article Online
View Journal | View Issue

Cite this: *Mater. Chem. Front.*, 2020, **4**, 3201

Mitochondria-anchoring and AIE-active photosensitizer for self-monitored cholangiocarcinoma therapy†

Tao Zhou,‡[a] Jianfang Zhu,‡[b] Dan Shang,‡[c] Chuxing Chai,[d] Youzhen Li,[e] Haiying Sun,[a] Yongqin Li,[a] Meng Gao *[e] and Min Li *[d]

Received 17th July 2020,
Accepted 1st September 2020

DOI: 10.1039/d0qm00503g

rsc.li/frontiers-materials

The morbidity of extrahepatic cholangiocarcinoma (CCA) has increased markedly in the past few decades. However, most patients with extrahepatic CCA are diagnosed at an advanced stage and thus cannot receive curative resection in time. To increase the long-term survival probability of nonresectable extrahepatic CCA patients, it is highly desirable to develop alternative treatment strategies. Photodynamic therapy is a highly efficient method for the ablation of cancer cells, but the conventional photosensitizers (PSs) suffer from self-quenching after local accumulation in organelles. To tackle this challenge, we herein develop a mitochondria-anchoring photosensitizer, **TTVPHE**, with aggregation-induced emission (AIE) characteristics for efficient ablation of extrahepatic CCA cells through the mitochondrial injury pathway. The **TTVPHE** probe shows significant advantages in terms of fast cell penetration ability, selective mitochondria-targeting ability, and excellent ROS generation ability under white light irradiation. Moreover, the probe can *in situ* monitor the mitochondrial injury process by translocation from mitochondria to the nuclear membrane. The ultrastructural changes in the morphology of mitochondria under PDT were also characterized using high resolution TEM. This AIE-active probe is promising for the treatment of advanced stage CCA.

Introduction

Cholangiocarcinoma (CCA) is a malignancy originating in the biliary tree and the morbidity has increased markedly in the past few decades.[1] Surgical resection is the only curative therapy for all subtypes of CCA in those who are good surgical candidates.[2] However, approximately 80% of CCA patients belong to the extrahepatic subtype and easily lose the opportunity for surgical excision due to the aggressiveness and late diagnosis of the extrahepatic subtype.[3,4] Moreover, chemotherapy or radiotherapy in the clinic cannot increase the long-term survival of patients with nonresectable extrahepatic CCA.[5] Therefore, the development of new therapy methods to improve the survival rate and life quality of extrahepatic CCA patients is an imperative task.

Photodynamic therapy (PDT) is a palliative and locoregional ablative treatment for extrahepatic CCA, and the first case of successful PDT for nonresectable CCA was reported by McCaughan's group in 1991.[6] To date, many clinic trials have demonstrated that PDT combined with biliary decompression can improve stent patency, survival, and quality of life for patients with nonresectable CCA.[7–11] The short life time of reactive oxygen species (ROS) requires the photosensitizers (PSs) to be accumulated at desired sites.[12,13] However, the conventional PSs, such as porphyrins and phthalocyanines, feature discotic structures and suffer from poor ROS generation efficiency at a high local concentration.[14–16] In contrast with the traditional PSs, the aggregation-induced emission fluorogens (AIEgens) with rotor structures have significant advantages in terms of high emission efficiency and photodynamic activity in the aggregate state.[17–25]

Mitochondria are the cell's energy sources, and mitochondria-targeted PSs could greatly improve the efficiency of photodynamic

[a] *Department of Otorhinolaryngology, Union Hospital, Tongji Medical College, Huazhong University of Science and Technology, Wuhan 430022, China*
[b] *Central Laboratory, Union Hospital, Tongji Medical College, Huazhong University of Science and Technology, Wuhan 430022, China*
[c] *Department of Vascular Surgery, Union Hospital, Tongji Medical College, Huazhong University of Science and Technology, Wuhan 430022, China*
[d] *Department of Hepatobiliary Surgery, Union Hospital, Tongji Medical College, Huazhong University of Science and Technology, Wuhan 430022, China. E-mail: liminmed@hust.edu.cn*
[e] *National Engineering Research Center for Tissue Restoration and Reconstruction, Key Laboratory of Biomedical Engineering of Guangdong Province, Key Laboratory of Biomedical Materials and Engineering of the Ministry of Education, Innovation Center for Tissue Restoration and Reconstruction, South China University of Technology, Guangzhou 510006, China. E-mail: msmgao@scut.edu.cn*

† Electronic supplementary information (ESI) available. See DOI: 10.1039/d0qm00503g

‡ These authors contributed equally to this work.

ablation of cancer cells.[26] Recently, mitochondria-targeted and AIE-active PSs with high ROS generation efficiency have shown great potential to kill cancer cells.[27–30] However, the ultrastructural changes in the morphology of mitochondria caused by PDT of the AIE-active PSs have been rarely investigated, which is critical for revealing of the therapeutic mechanism. Meanwhile, the uncontrollable cell death induced by ROS generation can lead to tumor lysis syndrome and metabolic derangements, including severe renal impairment, blood electrolyte disturbance, cardiac arrhythmias, and ultimately death.[31,32] Therefore, the development of mitochondria-targeted PSs with self-monitoring ability, which can precisely control the light treatment dose to avoid the excessive generation of ROS, is highly desirable. Recently, two AIE-active PSs were developed with self-monitoring ability, which could translocate from mitochondria to the nucleus and bind with nucleic acids during PDT treatment.[33,34] However, their ultimate binding with nucleic acids may lead to genotoxic, carcinogenic, and teratogenic risks.[35] To endow the AIE-active PSs with a safe self-monitoring ability, we herein develop an AIE-active PS, **TTVPHE**, which could not only efficiently destroy the mitochondria in cancer cells, but also *in situ* monitor the therapeutic process by translocating from the damaged mitochondria to the nuclear membrane. Moreover, the ultrastructural morphology of the damaged mitochondria was characterized using high resolution transmission electron microscopy (TEM). The AIE-active PS, **TTVPHE**, also has significant advantages of fast cell penetration ability in living cells, high intracellular retention ability after being hydrolysed by esterase, and excellent mitochondrial disruption ability through fast ROS generation. Based on these distinctive features, **TTVPHE** is promising for the treatment of advanced stage CCA.

Results and discussion

Synthesis of mitochondria-targeted AIE probes

The synthetic routes of **TTVPHE** and **TTVPHA** are shown in Scheme 1. The probe **TTVPHE** consists of a hydrophilic moiety of positively charged pyridinium (abbreviated as "P", red colour) and hydrophobic moieties of the (*E*)-4-(2-(5-(4-(diphenylamino)-phenyl)thiophen-2-yl)vinyl) group (abbreviated as "TTV", green colour), and 6-ethoxy-6-oxohexyl group (abbreviated as "HE", yellow colour). The positive charge and delocalized electrons of the lipophilic **TTVPHE** can facilitate its penetration into cells and selectively stain mitochondria with a negative membrane potential of ~−180 to 220 mV.[36] The compound **TTVPHA** with a hydrophilic carboxylic acid group was prepared as a control. The structures of **TTVPHE** and **TTVPHA** are well characterized and verified using NMR measurements (Fig. S1 and S2, ESI†).

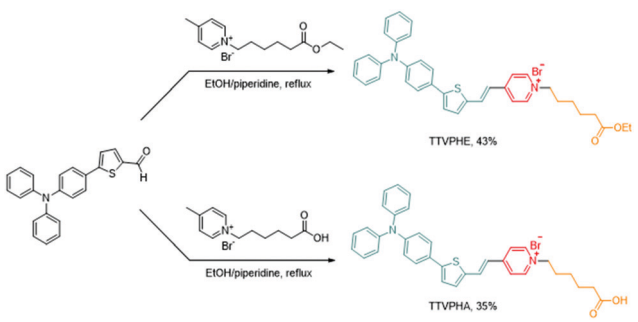

Scheme 1 The synthetic routes of **TTVPHE** and **TTVPHA**.

The investigation of photophysical properties

We then investigated the photophysical properties of **TTVPHE** and **TTVPHA** (Fig. 1A–F). Both **TTVPHE** and **TTVPHA** show typical electron-donating and -accepting (D–A) structural features, with the "TTV" moiety as the electron-donating group and the "P" moiety as the electron-accepting group, which will facilitate the red-shift emission based on a twisted intramolecular charge transfer (TICT) process. Moreover, the TTV moiety can freely rotate in solution with non-radiative relaxation as the predominant pathway, while the restriction of intramolecular motion in the aggregated state will facilitate the radiative relaxation associated with a strong emission. In DMSO solution, **TTVPHE** showed a maximum absorption wavelength at 482 nm and a very weak emission with a low quantum yield (Φ_F = 0.7%) due to the free intramolecular rotation and TICT effect. In DMSO/toluene mixture with increased toluene fractions (f_{Tol}), a gradually increased and blue-shifted emission was observed. When the f_{Tol} increased to 99%, a maximum emission wavelength at 596 nm was observed with an 80.24-fold increase in emission intensity and the Φ_F increased to 16.3%. These experiments verified the typical AIE properties of **TTVPHE**, which can be ascribed to the restriction of intramolecular motion and suppression of the TICT effect in the aggregate state. The compound **TTVPHA** also showed a typical AIE behaviour in DMSO/toluene mixture with increasing f_{Tol} from 0% to 90% with a 17.7-fold increase in emission intensity. However, the further increase of f_{Tol} from

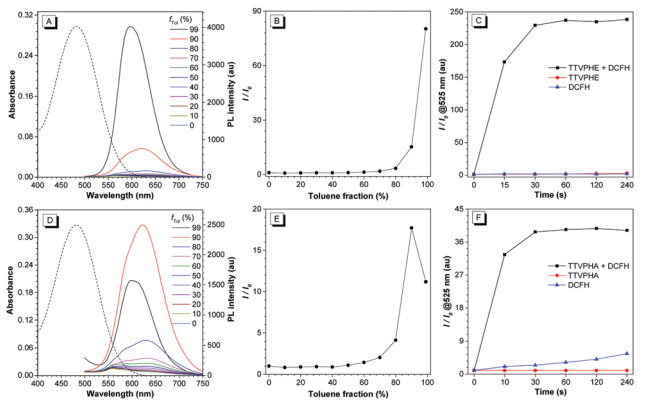

Fig. 1 (A) and (D) The normalized UV-vis absorption spectra (dashed line) of **TTVPHE** and **TTVPHA** in DMSO solution and their PL spectra in DMSO/toluene mixture with different toluene fractions (f_{Tol}); for **TTVPHE**, λ_{ex} = 482 nm; for **TTVPHA**, λ_{ex} = 478 nm. (B) and (E) The plots of the relative maximum emission intensity (I/I_0) of **TTVPHE** and **TTVPHA** *versus* the solvent composition of DMSO/toluene mixture. (C) and (F) The ROS generation of **TTVPHE** and **TTVPHA** in aqueous solution measured using DCFH under white light irradiation (10 mW cm^{-2}). [**TTVPHE**] = [**TTVPHA**] = 10 μM; [DCFH] = 10 μM; λ_{ex} = 488 nm, λ_{em} = 525 nm.

90% to 99% led to a blue-shifted emission from 621 to 599 nm with a 1.59-fold decrease in emission intensity, which can be ascribed to their different packing mode in the aggregate state.[37] Moreover, both **TTVPHE** and **TTVPHA** showed an excellent photodynamic activity (Fig. 1C and F), which was verified by the rapid turn-on fluorescence of an ROS indicator (2′-7′-dichlorodihydrofluorescein, DCFH) under white light irradiation (10 mW cm^{-2}).

Mitochondria-targeted imaging

Based on the high photostability of **TTVPHE** (Fig. S3, ESI†), the dynamic uptake process of **TTVPHE** and **TTVPHA** for extra-hepatic CCA QBC939 cells was monitored using confocal laser scanning microscope (CLSM). As shown in Fig. 2A, the **TTVPHE** first stained the cytoplasmic membrane within the initial 3 min, then it quickly penetrated into the cells and selectively accumulated in mitochondria. The **TTVPHA** probe as a comparison showed a much lower cellular uptake efficiency, which was verified using the fluorescence intensity and flow cytometry measurements (Fig. 2B and Fig. S4, S5, ESI†). The excellent cell penetration ability of **TTVPHE** could be ascribed to its lipophilic ethyl ester group with a higher hydrophobicity. After entry into cells, the **TTVPHE** could be hydrolyzed by esterase in the cytoplasm to *in situ* generate **TTVPHA** with a hydrophilic carboxylic group, which has a poor cytoplasmic membrane penetration ability, but a strong intracellular retention ability.[38] To further verify the mitochondria-targeting ability of **TTVPHE**, the QBC939 cells were further co-stained using a commercial mitochondrial dye MitoTracker Green (MTG). The red fluorescence signal from **TTVPHE** and the green fluorescence signal from MTG co-overlapped with a high Pearson's correlation coefficient of 0.96 (Fig. 2C and Fig. S6, ESI†), and their intensity profiles for the region of interest (ROI) line across QBC939 cells also varied in close synchrony (Fig. S7, ESI†). These results suggest that the **TTVPHE** probe has an excellent mitochondria-targeting ability. Because **TTVPHA** and **TTVPHE** are composed of a cationic pyridinium group "P" and a hydrophobic group "TTV", they can achieve selective accumulation in mitochondria with a high membrane potential (~−180 to 220 mV).[36] The cellular uptake process of **TTVPHE** and **TTVPHA** and their selective accumulation in mitochondria are intuitively illustrated in Fig. 2D.

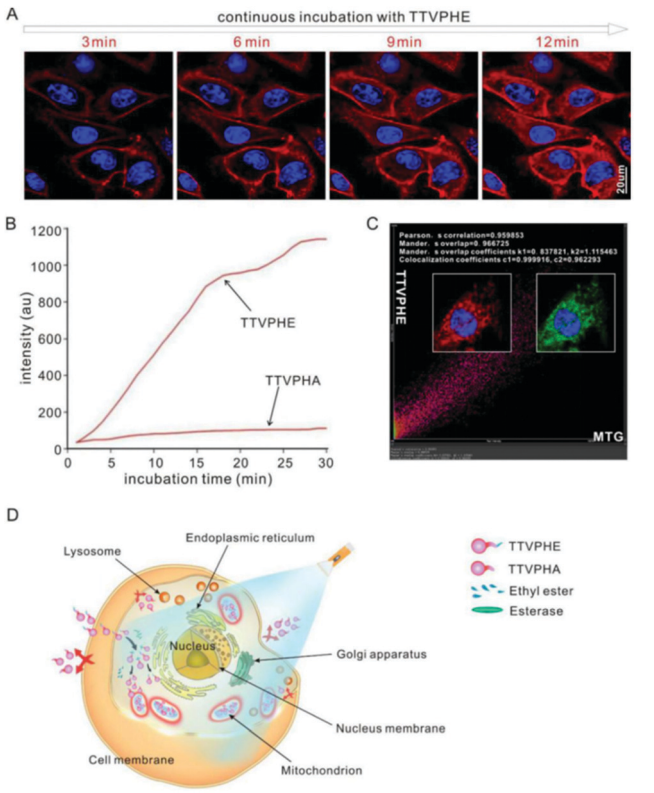

Fig. 2 The QBC939 cellular internalization enhanced by the additional ethyl ester group and mitochondria-targeting of **TTVPHE**. (A) The dynamic fluorescence images of the accumulation of **TTVPHE** in cells monitored using a CLSM. (B) The dynamic fluorescence intensity of cells continuously incubated with **TTVPHA** or **TTVPHE** and monitored using a CLSM. The intracellular fluorescence was analyzed using NIS-Elements Imaging Software. (C) The quantitation of mitochondrial localization of the cells co-stained with **TTVPHE** and MTG for 30 min. [**TTVPHE**] = [**TTVPHA**] = 5 μM, [MTG] = 50 nM. (D) The schematic illustration of the permeation into cells, hydrolysis by intracellular esterase and resistance to exudation of **TTVPHE**.

Photodynamic killing of cancer cells

We then investigated the photodynamic killing ability of **TTVPHE** for CCA cells. The fast penetration of **TTVPHE** into living cancer cells and the selective accumulation in mitochondria will greatly improve the photodynamic treatment efficacy. **TTVPHE** could efficiently generate ROS inside cells under white light irradiation, which was verified using the fast turn-on fluorescence of intracellular ROS indicator (2′-7′-chlorodihydrofluorescein diacetate, DCFH-DA) (Fig. 3A). It is noteworthy that a

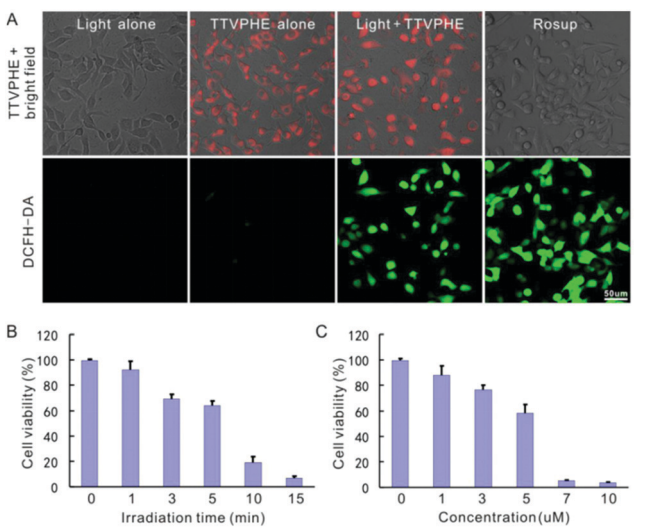

Fig. 3 (A) The intracellular ROS generation by incubation with **TTVPHE** (5 μM) under white light irradiation (2 min) was measured using DCFH-DA. The Rosup solution treatment was conducted as a positive control. (B) The time-dependent cytotoxicity by treatment with 5 μM **TTVPHE** under white light irradiation (180 mW cm^{-2}). (C) The **TTVPHE** concentration-dependent cytotoxicity under white light irradiation (180 mW cm^{-2}, 5 min).

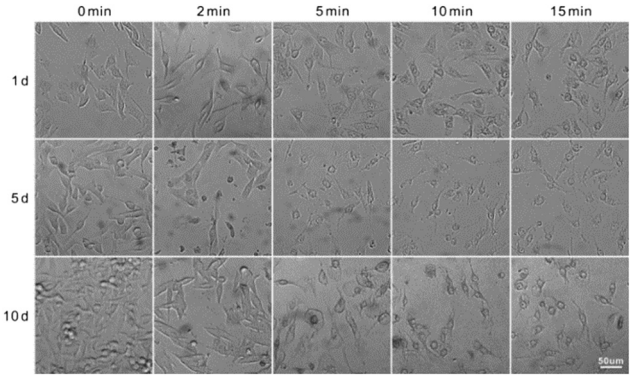

Fig. 4 The morphological changes in QBC939 cells after PDT treatment with **TTVPHE** (5 μM) for 0–15 min and further incubation for 1–10 d.

low cytotoxicity was observed for **TTVPHE** in the dark (Fig. S8, ESI†), which is critical to guarantee the selective killing of cancer cells with a high spatiotemporal resolution *via* light irradiation. The cytotoxicity of **TTVPHE** under light irradiation is closely related with the light dose and the incubation concentration. By prolonging the irradiation time to 15 min or increasing the concentration of **TTVPHE** to 7 μM, the cell viability decreased to almost zero, which clearly verified the photodynamic killing ability of **TTVPHE** through mitochondrial damage (Fig. 3B and C). Moreover, the changes in the cell morphology of QBC939 cells after PDT treatment with **TTVPHE** further verified the efficient inhibition of cancer cell growth (Fig. 4).

Mitochondria injury monitoring under PDT

Inspired by the excellent photodynamic activity of **TTVPHE**, we further investigated its mitochondria-targeted injury process. The morphology of mitochondria under PDT could be *in situ* monitored with an excellent contrast based on the high emission efficiency of **TTVPHE** in the aggregate state. As shown in Fig. 5A, the morphology of mitochondria changed from rod to swelling circles by prolonging the irradiation time from 0 to 15 min. Meanwhile, the nucleus membrane showed a gradual turn-on fluorescence, which suggests that the **TTVPHE** probe could translocate from damaged mitochondria to the nuclear membrane. Meanwhile, mitochondria in cells without light irradiation kept rod or sphere-shape and well-organized cristae. Furthermore, the changes in the ultrastructural morphology of mitochondria under PDT were characterized using high resolution TEM (Fig. 5B), which showed disorganized cristae and loss of matrix under light irradiation. An increased DNA fragmentation was also observed using the TUNEL assay under PDT by prolonging the irradiation time (Fig. 5C), which suggests that the ROS generation can efficiently induce cancer cell apoptosis.

Apoptosis caused by mitochondria-targeted PDT

To further verify the cancer cell apoptosis caused by ROS generation in mitochondria, the ROS quencher NAC was added as a control. After incubation with both **TTVPHE** and NAC, the mitochondrial morphology, characterized using CLSM and TEM, kept normal under light irradiation, which suggests that

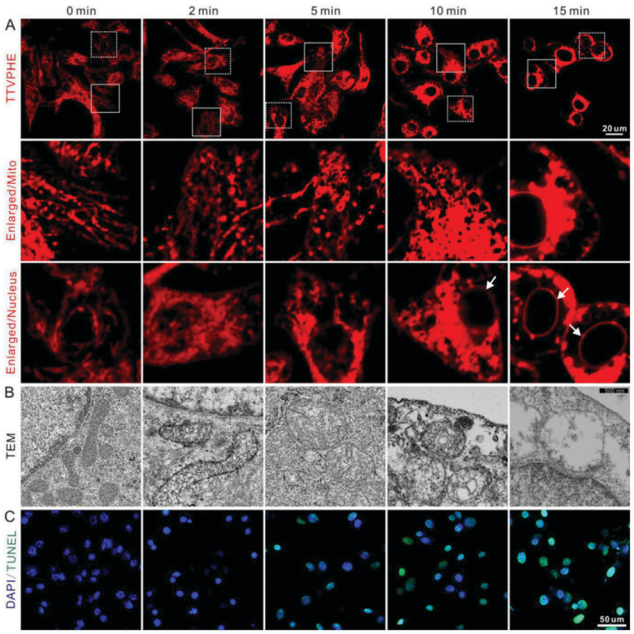

Fig. 5 (A) The CLSM images, (B) TEM images, and (C) TUNEL assay of QBC939 cells after white light irradiation for different time periods (180 mW cm^{-2}).

the generation of ROS is the predominant pathway for mitochondrial damage (Fig. 6A and C). Meanwhile, the mitochondrial membrane potential ($\Delta\psi_m$) measured by JC-1 showed that NAC could efficiently inhibit the decrease of $\Delta\psi_m$ under light irradiation (Fig. 6B). All these results suggest that the **TTVPHE** probe could efficiently destroy the mitochondrial structure and membrane potential. To determine whether the mitochondria-dependent apoptotic pathway was activated, Western blotting was conducted for the measurement of cytosolic cytochrome-*c* (Cyto *c*), and cleaved caspase-9 and caspase-3. As shown in Fig. 6D, their expression levels up-regulated significantly under light irradiation, and this tendency could be alleviated by the addition of NAC. These results verified that **TTVPHE** could efficiently activate the mitochondria-dependent apoptotic pathway.

Interestingly, the translocation of **TTVPHE** to the nuclear membrane at the late stage of PDT could also improve the nuclear membrane permeability *via* ROS generation under light irradiation. As shown in Fig. 6E, the live QBC939 cells were stained with a low dose of DAPI (1.0 μg mL^{-1}) for 2 h, but the DAPI dye distributed in the cytoplasm around the nucleus and could not penetrate through the nuclear membrane owing to its barrier function. On the contrary, DAPI could rapidly enter into the nucleus after the nucleus membrane was stained by **TTVPHE**, at the late stage of PDT treatment. Moreover, the TEM images of the nucleus before and after PDT treatment further verified the damaged nucleus structure (Fig. S9, ESI†). Therefore, the translocation of **TTVPHE** from damaged mitochondria to the nuclear membrane could further improve the PDT efficacy for efficient killing of cancer cells which is illustrated in Fig. 6F.

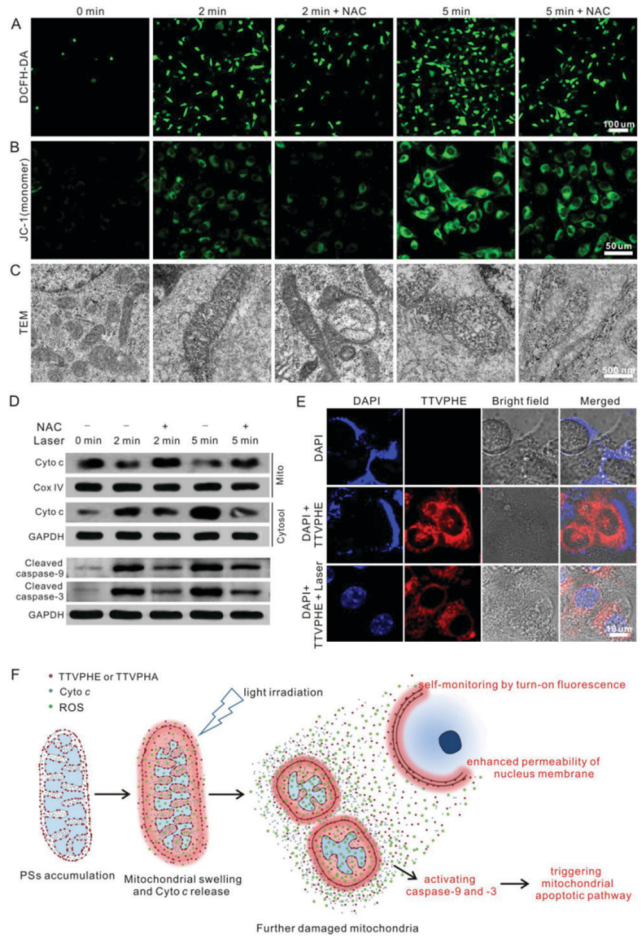

Fig. 6 (A) The intracellular ROS generation, (B) mitochondrial membrane potential ($\Delta\psi_m$), and (C) mitochondrial morphology were respectively measured using DCFH-DA, JC-1, and TEM in the absence and presence of NAC. (D) The western blot analysis of Cyto *c*, cleaved caspase-9 and caspase-3. (E) The CLSM images of QBC939 cells stained with DAPI, "DAPI + **TTVPHE**" without light irradiation, and "DAPI + **TTVPHE**" with light irradiation (180 mW cm^{-2}, 5 min). [DAPI] = 1 μg mL^{-1}; **TTVPHE** = 5 μM. (F) The schematic illustration of the mitochondrial apoptotic pathway, which can be self-monitored by the translocation of **TTVPHE** from damaged mitochondria to the nuclear membrane.

Conclusions

In conclusion, we have developed a mitochondria-anchoring and AIE-active PS, **TTVPHE**, which can not only selectively anchor in the mitochondria of CCA cells in a fast manner, but also *in situ* monitor the photodynamic process. At an early stage of PDT, changes in the morphology of mitochondria, which could be ascribed to the local accumulation of **TTVPHE** in the mitochondria at a high concentration, can be observed using high contrast fluorescence imaging. At a late stage of PDT, **TTVPHE** could translocate from the mitochondria to the nuclear membrane and further improve the PDT efficacy. It is noteworthy that the changes in the ultrastructural morphology of mitochondria under PDT were also characterized using high resolution TEM. We believe that this AIE-active probe will be promising for the photodynamic ablation of cancer cells with a high spatiotemporal resolution and excellent self-monitoring capability.

Experimental section

Materials and equipment

Ethyl 6-bromohexanoate and 4-methylpyridine were purchased from Aladdin (Shanghai, China), 6-bromohexanoic acid was purchased from Energy Chemical (Shanghai, China), 5-(4-(diphenylamino)phenyl)thiophene-2-carbaldehyde was purchased from Psai Chemical Products Co., Ltd (Henan, China), and piperidine was purchased from Kai Xin Logistics Co., Ltd (Guangdong, China). The commercial chemicals were directly used without further purification. QBC939 human extrahepatic cholangiocarcinoma cells were purchased from the Cell Bank of the Chinese Academy of Sciences (Shanghai, China). RPMI 1640 medium, fetal bovine serum (FBS) and JC-1 mitochondrial membrane potential probe were obtained from Thermo Fisher Scientific (Waltham, MA, USA). Penicillin–streptomycin mixture, trypsin and *N*-acetyl-L-cysteine (NAC) were bought from Sigma-Aldrich (Saint Louis, USA). Cell counting kit-8 (CCK8) was purchased from Dojindo Laboratories (Kumamoto, Japan). 2-(4-Amidinophenyl)-6-indolecarbamidine dihydrochloride (DAPI) and MitoTracker Green (MTG) were purchased from Yeasen Biotech Co., Ltd (Shanghai, China). 2′7′-Dichlorofluorescin diacetate (DCFH-DA) and the TUNEL apoptosis assay kit were obtained from Beyotime Institute of Biotechnology (Jiangsu, China). Cleaved caspase-9, cleaved caspase-3, cytochrome-*c* and Cox-IV antibodies were bought from Cell Signaling Technology (Danvers, MA, USA). RIPA, ECL substrate, GAPDH antibody, HRP-labeled anti-mouse secondary antibody, the BCA protein assay kit, and the mitochondria and nuclear protein extraction kits were purchased from Wuhan Servicebio Technology Co. Ltd (Wuhan, China).

UV-vis absorption spectra were measured using a Shimadzu UV-2600 spectrophotometer, at medium scanning rate, with quartz cuvettes of 1 cm path length. Photoluminescence spectra were recorded using a Horiba Fluoromax-4 spectrofluorometer. The absolute fluorescence quantum yield was measured using a Hamamatsu quantum yield spectrometer C11347 Quantaurus_QY. ^1H and ^{13}C NMR spectra were measured using a Bruker AV 500 NMR spectrometer. High resolution mass spectra (HRMS) were recorded using a Bruker maxis impact mass spectrometer operated in MALDI-TOF model.

Synthesis of TTVPHE and TTVPHA

1-(6-Ethoxy-6-oxohexyl)-4-methylpyridin-1-ium bromide (63.2 mg, 0.2 mmol) and 5-(4-(diphenylamino)phenyl)thiophene-2-carbaldehyde (71 mg, 0.2 mmol) were refluxed in ethanol (6 mL) under nitrogen and further added with piperidine (200 μL). The mixture was stirred at reflux under nitrogen for 1 h and then cooled to room temperature. The solvent was removed by rotary evaporation. The crude product was purified using silica-gel chromatography with CH_2Cl_2/CH_3OH = 10/1 as the eluent to afford **TTVPHE** as a red powder with 43% yield.

1-(5-Carboxypentyl)-4-methylpyridin-1-ium bromide (57.6 mg, 0.2 mmol) and 5-(4-(diphenylamino)phenyl)thiophene-2-carbaldehyde

(71 mg, 0.2 mmol) were dissolved in ethanol (6 mL) and further added with piperidine (200 μL). The mixture was stirred at reflux under nitrogen for 1 h and then cooled to room temperature. The solvent was removed by rotary evaporation. The crude product was purified using silica-gel chromatography with CH_2Cl_2/CH_3OH = 5/1 as the eluent to afford **TTVPHA** as a red powder with 35% yield.

Cell culture

QBC939 cells were cultured in RPMI 1640 medium supplemented with 10% FBS and 1% penicillin–streptomycin at 37 °C in a 5% CO_2, 90% relative humidity incubator.

Cell imaging

For cell imaging, the cells were first seeded in slide chambers and cultured overnight for adhesion, and then incubated with 5 μM **TTVPHE** or **TTVPHA**. Nuclei were labelled with DAPI (low dose of 1 μg mL^{-1}) overnight. After rising with PBS, the cells were imaged using a Confocal Laser Scanning Microscope (CLSM, Nikon Corporation, Japan). For **TTVPHE** and **TTVPHA**: λ_{ex} = 488 nm and band-pass filter λ = 552–617 nm. For DAPI: λ_{ex} = 405 nm and band-pass filter λ = 425–475 nm. To monitor the intracellular distribution of the **TTVPHE** or **TTVPHA**, the cell imaging was recorded using CLSM during incubation for 0 min to 30 min. The quantitative fluorescence intensity analysis was performed using Flow Cytometry (FCM, BD, CA, USA) after incubation with 5 μM **TTVPHE** or **TTVPHA** for 30 min.

For co-localization imaging, the cells were seeded in a 35 mm confocal dish and cultured overnight, and then incubated with 5 μM **TTVPHE** and 50 nM MTG for 30 min. After three washes, the cell images were taken using CLSM and the data were analyzed using NIS-Elements Imaging Software (Nikon Corporation, Japan) and Image-J (National Institutes of Health freeware, USA). For MTG: λ_{ex} = 488 nm and band-pass filter λ = 500–530 nm.

For cell morphology observation under photodynamic treatment, the cells were plated overnight and then incubated with 5 μM **TTVPHE** for 30 min. After replacement with fresh culture medium, the cells were exposed to white light irradiation (180 mW cm^{-2}) for 0, 2, 5, 10 and 15 min. Then, the cells were observed using CLSM. Furthermore, the cells were cultured and replaced with fresh culture medium every three days. As a control, the cells without light irradiation were sub-cultured every three days. The cell morphology was recorded using an optical microscope (Olympus IX71, Japan).

ROS detection

The ROS indicator, dichlorofluorescein (DCFH), was used to detect the ROS generation in solution under white light irradiation (10 mW cm^{-2}). Its stock solution (40 μM) in 1× PBS was prepared according to a procedure reported in the literature and further diluted to 2 μM in sample solution for measurement.[39] The PL spectra of 2,7-dichlorofluorescein (DCF) activated by **TTVPHE** or **TTVPHA** (10 μM) generated ROS under white light irradiation (10 mW cm^{-2}) was measured for different time intervals.

Intracellular ROS production was measured using the commercial probe DCFH-DA according to the manufacturer's instructions. After incubation in the presence or absence of **TTVPHE**, the cells were loaded with 10 μM DCFH-DA at 37 °C for 20 min in the dark. The cells were replaced with fresh medium and then exposed to white light irradiation at the power density of 180 mW cm^{-2}, then immediately imaged using CLSM. The cells incubated with 50 mg L^{-1} of a Rosup solution for 30 min were treated as the positive control. For DCFH: λ_{ex} = 488 nm and band-pass filter λ = 500–530 nm.

In vitro cytotoxicity

Cell viability after incubation with **TTVPHE** was evaluated using CCK8 assays. Briefly, the cells at a density of 1×10^4 were seeded into a 96-well plate overnight and then incubated with a series of concentrations of **TTVPHE** (0, 1, 3, 5, 7 and 10 μM). After treatment, the cells were incubated with 100 μL fresh medium including 10 μL CCK8 solution per well and further incubated for 4 h. The absorbance at 450 nm was measured using a Multimode Plate Reader (PerkinElmer Pte. Ltd, Singapore).

For studying the cytotoxicity induced by PDT, the cells were incubated with **TTVPHE** at different concentrations (0, 1, 3, 5, 7 and 10 μM) for 30 min and then exposed to white light irradiation (180 mW cm^{-2}). Then, the cells were incubated for 24 h and the cell viability was measured using a CCK8 assay. Moreover, the cell morphology was recorded using an optical microscope (Olympus IX71, Japan).

TEM analysis

The ultramicrostructural changes of mitochondria were observed using TEM according to the protocol of The Core Facility and Technical Support, Wuhan Institute of Virology (Wuhan, China). Briefly, after treatment with **TTVPHE** and light irradiation, the cells were fixed with 2.5% glutaraldehyde buffered in PBS for 2 h at room temperature. After washing three times with 0.1 M PBS, the cells were post-fixed in 1% osmium tetroxide at 4 °C for 2 h. And then the samples were dehydrated using ethanol solutions at a series of concentrations (30, 50, 70, 80, 85, 90, 95 and 100%), followed by permeation in a series of mixtures of acetone and epoxy resin (ratio of acetone and epoxy resin: 2 : 1, 1 : 1 and pure epoxy resin) at 37 °C. Finally, the samples were embedded and hardened in epoxy resin at 60 °C for 48 h, and then the ultrathin sections of 70 nm were cut using an EM UC7 ultramicrotome (Leica, Germany) and stained with uranyl acetate and lead citrate prior to analysis using a Tecnai G2 20 TWIN TEM (FEI Corporation, USA) operating at 200 kV.

TUNEL assay

The cell apoptosis was analyzed using a TUNEL assay kit according to the manufacturer's protocol. Briefly, the cells were treated with 5 μM **TTVPHE** for 30 min, and then replaced with fresh culture medium and then exposed to white light irradiation (180 mW cm^{-2}) for 0, 2, 5, 10 and 15 min, respectively. After further incubation for 24 h, the cells were fixed with

4% paraformaldehyde for 10 min and permeabilized with 0.3% Triton X-100 in PBS for 5 min at room temperature. After rinsing with PBS three times, the cells were incubated with TUNEL reaction mixture for 1 h at 37 °C in the dark. Finally, the nuclei were labelled with DAPI for 15 min and then the fluorescence was observed using CLSM.

Mitochondrial membrane potential ($\Delta\psi_m$) analysis

The $\Delta\psi_m$ was analyzed using JC-1 according to the manufacturer's protocol. The cells were incubated with 5 μM **TTVPHE** for 30 min and then 2 μg mL^{-1} of JC-1 for 20 min at 37 °C. To alleviate the mitochondrial injury, 10 μM NAC was co-incubated with **TTVPHE** for 30 min to quench the generated ROS from the PDT effect. After rinsing with PBS three times, the cell images were taken using CLSM. For JC-1(monomer): λ_{ex} = 488 nm and band-pass filter λ = 500–530 nm.

Western blotting analysis

The cells were incubated with 5 μM **TTVPHE** for 30 min. After PDT treatment, the cytosolic and mitochondrial proteins were extracted using mitochondria and nuclear protein extraction kits, respectively. The total protein was extracted using a RIPA lysis buffer. The protein concentration was measured using a BCA protein assay kit. Then equivalent amounts of protein were loaded in the wells of sodium dodecyl sulfate-polyacrylamide gel electrophoresis (SDS-PAGE) and separated by gel electrophoresis. After being transferred onto PVDF membranes and blocked using 5% non-fat milk for 1 h, the proteins were incubated with primary antibodies overnight at 4 °C. Primary antibodies included anti-Cyto *c* (1:200), anti-Cox IV (1:500), anti-cleaved caspase-9 (1:500), anti-cleaved caspase-3 (1:500) and anti-GAPDH antibody (1:1000). Then, they were incubated with HRP-conjugated secondary antibodies, and the immunoreactivity was detected using an ECL substrate and recorded using the ChemiDoc imaging system (Bio-Rad, Hercules, USA).

Conflicts of interest

There are no conflicts to declare.

Acknowledgements

This work was financially supported by the National Natural Science Foundation of China (81874208, 81771005, 21788102, 31771098, 51620105009, 21877040, U1801252), Natural Science Foundation of Hubei Province (2017CFB623, 2015CFB527), the Science and Technology Planning Project of Guangzhou (201804020060, 201607020015 and 201704030069), Pearl River S&T Nova Program of Guangzhou (201806010152), Natural Science Foundation of Guangdong Province (2020B1515020010 and 2016A030312002) and the Fundamental Research Funds for the Central Universities (2018JQ01, 2014QN064). The authors would like to thank Pei Zhang and An-na Du from The Core Facility and Technical Support, Wuhan Institute of Virology, for their help in producing TEM micrographs.

Notes and references

1 J. M. Banales, V. Cardinale, G. Carpino, M. Marzioni, J. B. Andersen, P. Invernizzi, G. E. Lind, T. Folseraas, S. J. Forbes, L. Fouassier, A. Geier, D. F. Calvisi, J. C. Mertens, M. Trauner, A. Benedetti, L. Maroni, J. Vaquero, R. I. Macias, C. Raggi, M. J. Perugorria, E. Gaudio, K. M. Boberg, J. J. Marin and D. Alvaro, Expert consensus document: Cholangiocarcinoma: current knowledge and future perspectives consensus statement from the European Network for the Study of Cholangiocarcinoma (ENS-CCA), *Nat. Rev. Gastroenterol. Hepatol.*, 2016, **13**, 261–280.

2 N. Razumilava and G. J. Gores, Cholangiocarcinoma, *Lancet*, 2014, **383**, 2168–2179.

3 S. Rizvi, S. A. Khan, C. L. Hallemeier, R. K. Kelley and G. J. Gores, Cholangiocarcinoma - evolving concepts and therapeutic strategies, *Nat. Rev. Clin. Oncol.*, 2018, **15**, 95–111.

4 B. Blechacz and G. J. Gores, Cholangiocarcinoma: advances in pathogenesis, diagnosis, and treatment, *Hepatology*, 2008, **48**, 308–321.

5 T. Patel, Cholangiocarcinoma-controversies and challenges, *Nat. Rev. Gastroenterol. Hepatol.*, 2011, **8**, 189–200.

6 J. S. McCaughan, Jr, B. F. Mertens, C. Cho, R. D. Barabash and H. W. Payton, Photodynamic Therapy to Treat Tumors of the Extrahepatic Biliary Ducts: A Case Report, *JAMA Surg.*, 1991, **126**, 111–113.

7 M. A. Ortner, J. Liebetruth, S. Schreiber, M. Hanft, U. Wruck, V. Fusco, J. M. Muller, H. Hortnagl and H. Lochs, Photodynamic therapy of nonresectable cholangiocarcinoma, *Gastroenterology*, 1998, **114**, 536–542.

8 M. E. Ortner, K. Caca, F. Berr, J. Liebetruth, U. Mansmann, D. Huster, W. Voderholzer, G. Schachschal, J. Mossner and H. Lochs, Successful photodynamic therapy for nonresectable cholangiocarcinoma: a randomized prospective study, *Gastroenterology*, 2003, **125**, 1355–1363.

9 A. Wagner, U. W. Denzer, D. Neureiter, T. Kiesslich, A. Puespoeck, E. A. Rauws, K. Emmanuel, N. Degenhardt, U. Frick, U. Beuers, A. W. Lohse, F. Berr and G. W. Wolkersdorfer, Temoporfin improves efficacy of photodynamic therapy in advanced biliary tract carcinoma: A multicenter prospective phase II study, *Hepatology*, 2015, **62**, 1456–1465.

10 H. Moole, H. Tathireddy, S. Dharmapuri, V. Moole, R. Boddireddy, P. Yedama, S. Dharmapuri, A. Uppu, N. Bondalapati and A. Duvvuri, Success of photodynamic therapy in palliating patients with nonresectable cholangiocarcinoma: A systematic review and meta-analysis, *World J. Gastroenterol.*, 2017, **23**, 1278–1288.

11 W. Dolak, H. Schwaighofer, B. Hellmich, B. Stadler, G. Spaun, W. Plieschnegger, A. Hebenstreit, J. Weber-Eibel, F. Siebert, K. Emmanuel, P. Knoflach, M. Gschwantler, W. Vogel, M. Trauner, A. Puspok and for the Austrian PDT study group, Photodynamic therapy with polyhematoporphyrin for malignant biliary obstruction: A nationwide retrospective study of 150 consecutive applications, *United Eur. Gastroenterol. J.*, 2017, **5**, 104–110.

12 J. Yang, J. Dai, Q. Wang, Y. Cheng, J. Guo, Z. Zhao, Y. Hong, X. Lou and F. Xia, Tumor Triggered Disassembly of Multiple-

Agent-Therapy Probe for Efficient Cellular Internalization, *Angew. Chem., Int. Ed.*, 2020, DOI: 10.1002/anie.202009196.

13 X. Guo, B. Cao, C. Wang, S. Lu and X. Hu, *In vivo* photothermal inhibition of methicillin-resistant Staphylococcus aureus infection by in situ templated formulation of pathogen-targeting phototheranostics, *Nanoscale*, 2020, **12**, 7651–7659.

14 M.-C. Hsieh, C.-H. Chien, C.-C. Chang and T.-C. Chang, Aggregation induced photodynamic therapy enhancement based on linear and nonlinear excited FRET of fluorescent organic nanoparticles, *J. Mater. Chem. B*, 2013, **1**, 2350.

15 C. A. Robertson, D. H. Evans and H. Abrahamse, Photodynamic therapy (PDT): a short review on cellular mechanisms and cancer research applications for PDT, *J. Photochem. Photobiol., B*, 2009, **96**, 1–8.

16 A. P. Castano, T. N. Demidova and M. R. Hamblin, Mechanisms in photodynamic therapy: part one—photosensitizers, photochemistry and cellular localization, *Photodiagn. Photodyn. Ther.*, 2004, **1**, 279–293.

17 M. Li, Y. Gao, Y. Yuan, Y. Wu, Z. Song, B. Z. Tang, B. Liu and Q. C. Zheng, One-Step Formulation of Targeted Aggregation-Induced Emission Dots for Image-Guided Photodynamic Therapy of Cholangiocarcinoma, *ACS Nano*, 2017, **11**, 3922–3932.

18 Y. Gao, Q. C. Zheng, S. Xu, Y. Yuan, X. Cheng, S. Jiang, Kenry, Q. Yu, Z. Song, B. Liu and M. Li, Theranostic Nanodots with Aggregation-Induced Emission Characteristic for Targeted and Image-Guided Photodynamic Therapy of Hepatocellular Carcinoma, *Theranostics*, 2019, **9**, 1264–1279.

19 F. Xia, J. Wu, X. Wu, Q. Hu, J. Dai and X. Lou, Modular Design of Peptide- or DNA-Modified AIEgen Probes for Biosensing Applications, *Acc. Chem. Res.*, 2019, **52**, 3064–3074.

20 S. Xu, Y. Duan and B. Liu, Precise Molecular Design for High-Performance Luminogens with Aggregation-Induced Emission, *Adv. Mater.*, 2020, **32**, e1903530.

21 M. Gao and B. Z. Tang, AIE-based cancer theranostics, *Coord. Chem. Rev.*, 2020, **402**, 213076.

22 J. Dai, Y. Li, Z. Long, R. Jiang, Z. Zhuang, Z. Wang, Z. Zhao, X. Lou, F. Xia and B. Z. Tang, Efficient Near-Infrared Photosensitizer with Aggregation-Induced Emission for Imaging-Guided Photodynamic Therapy in Multiple Xenograft Tumor Models, *ACS Nano*, 2020, **14**, 854–866.

23 Y. Gao, H. Zhang, Z. He, F. Fang, C. Wang, K. Zeng, S. Gao, F. Meng, L. Luo and B. Z. Tang, Multicationic AIEgens for unimolecular photodynamic theranostics and two-photon fluorescence bioimaging, *Mater. Chem. Front.*, 2020, **4**, 1623–1633.

24 Q. Wan, R. Zhang, Z. Zhuang, Y. Li, Y. Huang, Z. Wang, W. Zhang, J. Hou and B. Z. Tang, Molecular Engineering to Boost AIE-Active Free Radical Photogenerators and Enable High-Performance Photodynamic Therapy under Hypoxia, *Adv. Funct. Mater.*, 2020, DOI: 10.1002/adfm.202002057.

25 W. Zhang, Y. Huang, Y. Chen, E. Zhao, Y. Hong, S. Chen, J. W. Y. Lam, Y. Chen, J. Hou and B. Z. Tang, Amphiphilic Tetraphenylethene-Based Pyridinium Salt for Selective Cell-Membrane Imaging and Room-Light-Induced Special Reactive Oxygen Species Generation, *ACS Appl. Mater. Interfaces*, 2019, **11**, 10567–10577.

26 W. Zhang, X. Hu, Q. Shen and D. Xing, Mitochondria-specific drug release and reactive oxygen species burst induced by polyprodrug nanoreactors can enhance chemotherapy, *Nat. Commun.*, 2019, **10**, 1704.

27 M. Jiang, R. T. K. Kwok, X. Li, C. Gui, J. W. Y. Lam, J. Qu and B. Z. Tang, A simple mitochondrial targeting AIEgen for image-guided two-photon excited photodynamic therapy, *J. Mater. Chem. B*, 2018, **6**, 2557–2565.

28 D. Wang, M. M. S. Lee, G. Shan, R. T. K. Kwok, J. W. Y. Lam, H. Su, Y. Cai and B. Z. Tang, Highly Efficient Photosensitizers with Far-Red/Near-Infrared Aggregation-Induced Emission for *In Vitro* and *In Vivo* Cancer Theranostics, *Adv. Mater.*, 2018, e1802105.

29 D. Wang, H. Su, R. T. K. Kwok, X. Hu, H. Zou, Q. Luo, M. M. S. Lee, W. Xu, J. W. Y. Lam and B. Z. Tang, Rational design of a water-soluble NIR AIEgen, and its application in ultrafast wash-free cellular imaging and photodynamic cancer cell ablation, *Chem. Sci.*, 2018, **9**, 3685–3693.

30 H. Yang, J. Zhuang, N. Li, Y. Li, S. Zhu, J. Hao, J. Xin and N. Zhao, Efficient near-infrared photosensitizer with aggregation-induced emission characteristics for mitochondria-targeted and image-guided photodynamic cancer therapy, *Mater. Chem. Front.*, 2020, **4**, 2064–2071.

31 A. E. Mirrakhimov, P. Voore, M. Khan and A. M. Ali, Tumor lysis syndrome: A clinical review, *World J Crit. Care Med.*, 2015, **4**, 130–138.

32 U. Durani, N. D. Shah and R. S. Go, In-Hospital Outcomes of Tumor Lysis Syndrome: A Population-Based Study Using the National Inpatient Sample, *Oncologist*, 2017, **22**, 1506–1509.

33 T. Zhang, Y. Li, Z. Zheng, R. Ye, Y. Zhang, R. T. K. Kwok, J. W. Y. Lam and B. Z. Tang, In Situ Monitoring Apoptosis Process by a Self-Reporting Photosensitizer, *J. Am. Chem. Soc.*, 2019, **141**, 5612–5616.

34 Y. Gao, X. Wang, X. He, Z. He, X. Yang, S. Tian, F. Meng, D. Ding, L. Luo and B. Z. Tang, A Dual-Functional Photosensitizer for Ultraefficient Photodynamic Therapy and Synchronous Anticancer Efficacy Monitoring, *Adv. Funct. Mater.*, 2019, **29**, 1902673.

35 Y. Hong, S. Chen, C. W. T. Leung, J. W. Y. Lam and B. Z. Tang, Water-Soluble Tetraphenylethene Derivatives as Fluorescent "Light-Up" Probes for Nucleic Acid Detection and Their Applications in Cell Imaging, *Chem. – Asian J.*, 2013, **8**, 1806–1812.

36 L. B. Chen, Mitochondrial membrane potential in living cells, *Annu. Rev. Cell Biol.*, 1988, **4**, 155–181.

37 A. Shao, Y. Xie, S. Zhu, Z. Guo, S. Zhu, J. Guo, P. Shi, T. D. James, H. Tian and W.-H. Zhu, Far-Red and Near-IR AIE-Active Fluorescent Organic Nanoprobes with Enhanced Tumor-Targeting Efficacy: Shape-Specific Effects, *Angew. Chem., Int. Ed.*, 2015, **54**, 7275–7280.

38 P. Breeuwer, J. L. Drocourt, N. Bunschoten, M. H. Zwietering, F. M. Rombouts and T. Abee, Characterization of uptake and hydrolysis of fluorescein diacetate and carboxyfluorescein diacetate by intracellular esterases in Saccharomyces cerevisiae, which result in accumulation of fluorescent product, *Appl. Environ. Microbiol.*, 1995, **61**, 1614–1619.

39 L. Bourre, S. Thibaut, A. Briffaud, N. Rousset, S. Eleouet, Y. Lajat and T. Patrice, Indirect detection of photosensitizer ex vivo, *J. Photochem. Photobiol., B*, 2002, **67**, 23–31.

